Nano Research

Open Access

Research Article

Carbon dots-assisted cobalt ions anchored on graphitic carbon nitride enables highly efficient photocatalytic CO_2 conversion

Sudi Chen[1], Jiajia Wei[2], Tao Wang[2], Shuanghong Liu[1], Shufang Tian[2] ✉, and Feng Bai[1] ✉

[1] *Key Laboratory for Special Functional Materials of Ministry of Education, National & Local Joint Engineering Research Center for High-efficiency Display and Lighting Technology, School of Nanoscience and Materials Engineering, Collaborative Innovation Center of Nano Functional Materials and Applications, Henan University, Kaifeng 475004, China*

[2] *Henan Key Laboratory of Quantum Materials and Quantum Energy, School of Future Technology, Henan University, Zhengzhou 450046, China*

Cite this article: *Nano Research*, **2026**, *19*, 94908500. https://doi.org/10.26599/NR.2026.94908500

ABSTRACT: Artificial photosynthesis that converts solar energy and CO_2 into value-added chemicals such as CO represents a highly promising route for sustainable energy production. However, the inherent limitations of graphitic carbon nitride (g-C_3N_4), including the lack of efficient active sites and sluggish charge transfer, significantly hinder its photocatalytic CO_2 reduction performance. Herein, a novel strategy is proposed in which amino-functionalized carbon dots (pCDs) mediate the construction of Co-N coordination active centers on g-C_3N_4 nanosheets (Co-5pCDs-g-C_3N_4). Advanced characterizations reveal that Co ions are anchored on the surface of the pCDs through Co-N coordination with amino groups, while the structural incorporation of the pCDs effectively reduces the lateral dimensions of the g-C_3N_4 nanosheets. This structural design markedly enhances charge-carrier separation within Co-5pCDs-g-C_3N_4, promotes charge migration toward the Co-N active centers, and enables highly selective CO_2 to CO conversion. Notably, Co-5pCDs-g-C_3N_4 achieves a remarkable CO production rate of 616.1 μmol·g^{-1}·h^{-1}, 91 times higher than Co-g-C_3N_4 with a CO selectivity of 92%. Femtosecond transient absorption (fs-TA) spectroscopy provides crucial mechanistic insights into the improved performance. The incorporation of pCDs significantly prolongs the average lifetime of photogenerated charge carriers, whereas the introduction of Co further extends this lifetime by promoting charge separation and suppressing recombination. Owing to the dual functions of pCDs in modulating charge dynamics and tailoring the coordination environment, the resulting catalyst demonstrates markedly enhanced photocatalytic CO_2 reduction performance, underscoring its strong potential for advanced solar-driven catalytic applications.

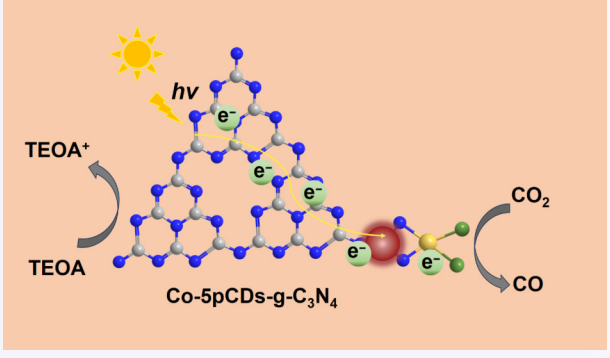

KEYWORDS: carbon dots, graphitic carbon nitride, photocatalysis, CO_2 conversion, charge carrier dynamics

1 Introduction

Efficient carbon capture and utilization are urgently needed to address rising CO_2 emissions and mitigate climate change [1, 2]. Solar-driven photocatalytic CO_2 conversion, mimicking natural photosynthesis, offers a promising route for carbon neutrality and renewable energy use [3]. However, current photocatalysts suffer from low efficiency and poor stability, limiting their practical applications [4–6]. Developing catalysts with high activity, stability, and scalability is therefore crucial.

Among various photocatalytic materials, graphitic carbon nitride (g-C_3N_4) has attracted considerable attention due to its suitable bandgap, excellent chemical and thermal stability, earth-abundant composition, and facile synthesis [7–11]. However, bulk g-C_3N_4 still suffers from a high exciton binding energy, limited specific surface area, and rapid recombination of photogenerated charge carriers, all of which severely restrict its efficiency in photocatalytic CO_2 reduction [12]. To address these limitations, numerous strategies involving structural and electronic modulation have been proposed to enhance its light-harvesting ability and charge separation efficiency [13, 14]. Typical modification approaches include

Received: November 30, 2025; **Revised:** January 24, 2026
Accepted: January 28, 2026

✉Address correspondence to Shufang Tian, tianshufang@henu.edu.cn; Feng Bai, baifengsun@126.com

morphology engineering to enlarge the reactive interface and shorten charge migration paths, as well as doping [15–20], morphology control [21, 22], or heterojunction construction to promote charge transport [23–25]. Among these modification strategies, carbon dots (CDs) engineering has demonstrated distinct advantages in photocatalytic systems, owing to their excellent electron-mediating and reservoir capabilities, co-catalytic functions, and abundant surface functional groups [26–28]. CDs typically consist of a crystalline carbon core and a functionalized shell, enabling them to serve as electron mediators or cocatalysts in photocatalytic processes, thereby extending the light absorption range and suppressing electron–hole recombination [29–32]. The surface functional groups of CDs act as electron-transfer "bridges", forming covalent connections between the photosensitive units and the carbon core, thereby accelerating electron migration and enhancing the overall photocatalytic efficiency. Meanwhile, these functional groups can also coordinate metal ions [33–35]. Especially, metal-nitrogen/oxygen (M-N/O) coordination environments are capable of activating small molecules such as CO_2 and O_2 through hydrogen bonding, metal-CO_2 coordination, or van der Waals interactions, and thus have been widely recognized as highly active sites for CO_2 reduction [36–40]. However, many previously reported strategies that rely on g-C_3N_4 substrates to anchor catalytic active centers suffer from intrinsic limitations such as severe charge-carrier recombination, sluggish charge migration, and low metal-ion loading [41–43]. Therefore, simply introducing metal species into pristine g-C_3N_4 may not achieve efficient charge separation while simultaneously maximizing the enhancement of photocatalytic performance.

In this work, *p*-phenylenediamine (PPD) was used as the precursor to synthesize CDs rich in $-NH_2$ functional groups, which were subsequently copolymerized with urea via a thermal polymerization process to establish covalent linkages between the amino-functionalized carbon dots (pCDs) and the g-C_3N_4 framework. As shown in Fig. 1, the amino groups on the surface of pCDs can effectively anchor Co ions, enabling the formation of well-defined Co-N coordination environments on g-C_3N_4 nanosheets (Co-5pCDs-g-C_3N_4), which are expected to enhance catalytic activity. Benefiting from favorable energy-level alignment, photogenerated electrons can migrate from g-C_3N_4 to the crystalline pCDs core for temporary storage, and subsequently transfer to Co active sites coordinated with surface functional groups, thereby facilitating the photocatalytic reduction of CO_2. Photoluminescence (PL) and electrochemical measurements demonstrate that the introduction of pCDs and cobalt ions significantly enhances the separation of photogenerated charge carriers. Femtosecond transient absorption (fs-TA) spectroscopy at 650 nm further elucidates the carrier dynamics: The incorporation of pCDs increases the average lifetime of photogenerated carriers from 53.27 to 74.19 ps, while the cooperative effect of Co ions suppresses recombination and enhances charge-separation efficiency, thereby extending the lifetime to 122.77 ps. Benefiting from the dual functions of pCDs in modulating charge dynamics and tailoring the coordination environment, the resulting catalyst exhibits markedly improved photocatalytic CO_2 reduction activity. Co-5pCDs-g-C_3N_4 achieves a CO production rate of 616.1 $\mu mol \cdot g^{-1} \cdot h^{-1}$, 91 times higher than Co-g-C_3N_4 and with a CO selectivity of 92%. In addition, Co-5pCDs-g-C_3N_4 shows excellent recyclability, as its original catalytic performance can be fully restored after simple re-metalation over five consecutive cycles. This work provides a new design strategy for tuning cobalt coordination structures via CDs engineering, thereby substantially boosting the CO_2 reduction performance of g-C_3N_4-based photocatalysts.

2 Experimental

2.1 Chemical reagents

PPD was obtained from Adamas-beta. Urea and acetonitrile (CH_3CN) were acquired from J&K Scientific, and triethanolamine (TEOA) was purchased from Aladdin. Dehydrated ethanol (EtOH) was provided by Tianjin Fuyu Fine Chemical Co., Ltd. $CoCl_2 \cdot 6H_2O$ and $^{13}CO_2$ were obtained from Sigma-Aldrich. All chemicals were used without further purification. Ultrapure water (18.2 MΩ·cm) was produced by a Barnstead Nanopure water purification system.

2.2 Fabrication of catalysts

2.2.1 *Preparation of pCDs*

200 mg of PPD was dissolved in 20 mL of EtOH using ultrasonic treatment. The homogeneous solution was then transferred into a 100 mL of polytetrafluoroethylene (PTFE)-lined autoclave and heated at 180 °C for 12 h. Upon completion of the reaction, pCDs were obtained with a concentration of 10 $mg \cdot mL^{-1}$.

2.2.2 *Preparation of g-C_3N_4*

To prepare the powdered g-C_3N_4 sample, 20 g of urea was weighed into a crucible and loosely covered with aluminum foil to allow for gas exchange. The crucible was then transferred to a muffle furnace and heated to 550 °C using a programmed heating rate of 3 $°C \cdot min^{-1}$. After maintaining this temperature for 2 h, the sample was allowed to cool naturally to room temperature.

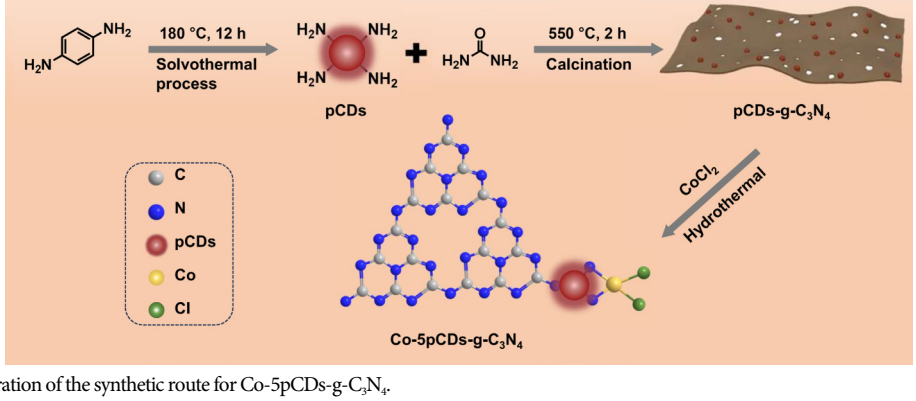

Figure 1 Schematic illustration of the synthetic route for Co-5pCDs-g-C_3N_4.

2.2.3 *Synthesis of xpCDs-g-C_3N_4*

The *x*pCDs-g-C_3N_4 samples were synthesized by thoroughly mixing 20 g of urea with *x* mg of pCDs (*x* = 1, 2.5, 5, or 10) solution, followed by grinding the mixture in a mortar. The homogeneous powder was then transferred to a crucible and calcined at 550 °C for 2 h with a heating rate of 3 °C·min^{-1}.

2.2.4 *Preparation of Co-xpCDs-g-C_3N_4*

A mixture of 50 mg of *x*pCDs-g-C_3N_4 was dispersed in 10 mL of deionized water and sonicated for 30 min. Whereafter, 5 mg of $CoCl_2·6H_2O$ was added, and the solution was further sonicated for 15 min before being transferred to a 15 mL PTFE vial. The reaction was carried out at 100 °C for 12 h. After cooling to room temperature, the product was washed three times with water and once with EtOH, followed by oven drying. The resulting samples were labeled as Co-*x*pCDs-g-C_3N_4 (*x* = 1, 2.5, 5, or 10).

3 Results and discussion

3.1 Synthesis and characterization

The transmission electron microscopy (TEM) image (Fig. 2(a)) reveals that the pCDs exhibit a nearly spherical morphology with high monodispersity, and the statistical analysis of 100 individual nanoparticles (inset in Fig. 2(a)) indicates a particle size distribution ranging from 2.00 to 4.29 nm, with an average diameter of 2.92 nm. Furthermore, the high-resolution TEM (HRTEM) image (Fig. S1 in the Electronic Supplementary Material (ESM)) displays clear lattice fringes with an interplanar spacing of 0.21 nm, corresponding to the (100) plane of graphitic carbon [44]. The optical absorption properties of the pCDs were analyzed by ultraviolet–visible (UV–vis) spectroscopy. As shown in Fig. S2 in the ESM, the pCDs exhibit a strong characteristic absorption at 208 nm, attributed to the π–π* transition of C=C bonds in aromatic domains, along with a weaker and broader band around 430 nm, arising from the n–π* transition of C=N bonds, further confirming the successful synthesis of the CDs [45]. To characterize the surface functionalities of the pCDs, Fourier transform infrared (FT-IR) spectroscopy was employed. As shown in Fig. S3 in the ESM, the sharp peak at 1512 cm^{-1} is assigned to the C=C skeletal vibration, while the peak at 1253 cm^{-1} corresponds to the C–N stretching vibration. The distinct feature at 1607 cm^{-1} can be attributed to the stretching vibration of the C=N bond. Moreover, the broad peak in the range of 3000–3500 cm^{-1} arises from the stretching vibrations of –NH_2 groups [46]. These results confirm that the synthesized CDs are rich in –NH_2 functional groups.

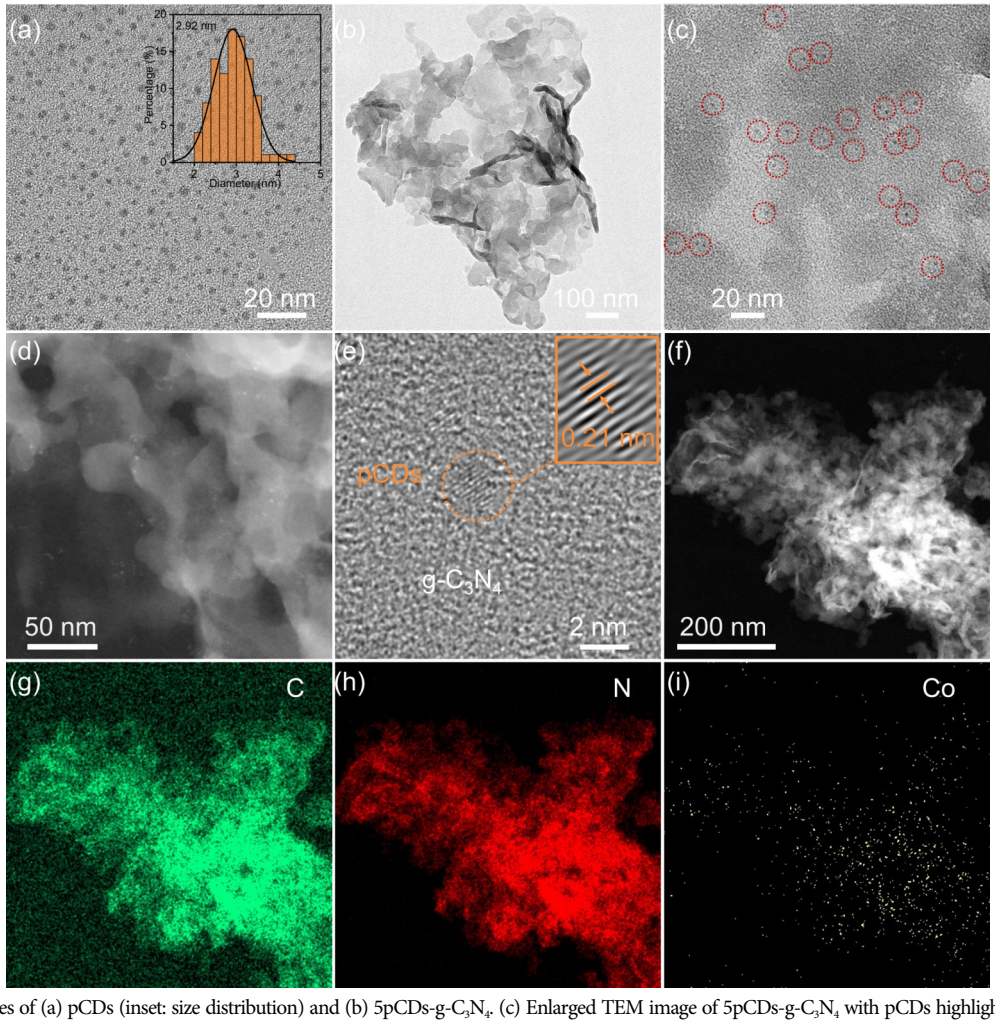

Figure 2 TEM images of (a) pCDs (inset: size distribution) and (b) 5pCDs-g-C_3N_4. (c) Enlarged TEM image of 5pCDs-g-C_3N_4 with pCDs highlighted by red circles. (d) TEM dark-field image showing bright pCDs in 5pCDs-g-C_3N_4. (e) HRTEM image of 5pCDs-g-C_3N_4 (inset: lattice fringes of 5pCDs-g-C_3N_4). (f)–(i) Elemental mapping of Co-5pCDs-g-C_3N_4 for C, N, and Co.

To further investigate the coordination interaction between surface amino groups of the pCDs and cobalt ions, the optical properties of pCDs with varying concentrations of Co ions were examined by PL spectroscopy [47, 48]. As shown in Fig. S4 in the ESM, the PL spectrum of pCDs exhibits a distinct emission peak at 600 nm under an excitation wavelength of 400 nm. With increasing cobalt ion concentration, the fluorescence intensity progressively decreases, whereas the blank control shows negligible change, indicating that the surface amino groups of pCDs can effectively interact with cobalt ions, leading to fluorescence quenching.

Subsequently, the as-prepared pCDs and urea were thermally copolymerized via a top-down approach to obtain pCDs-g-C_3N_4. The morphology and structure of the as-prepared pCDs-g-C_3N_4 samples were investigated by scanning electron microscopy (SEM) and TEM. SEM (Fig. S5(a) in the ESM) and TEM images (Fig. 2(b)) show that 5pCDs-g-C_3N_4 retains the sheet-like structure of pristine g-C_3N_4 (Fig. S6 in the ESM), while the introduction of pCDs leads to a significant reduction in nanosheet size. TEM observations further confirm the porous architecture, with dark pCDs clearly visible on the surface of 5pCDs-g-C_3N_4 (highlighted by circles in Fig. 2(c) and Fig. S5(b) in the ESM). Nevertheless, the chemical composition of the pCDs is similar to that of g-C_3N_4, resulting in comparable contrast and making it difficult to accurately determine the pCDs concentration in conventional TEM images, especially over larger fields of view. The higher crystallinity of the pCDs, yet, allows them to be more readily distinguished from g-C_3N_4 in the TEM dark-field images of 5pCDs-g-C_3N_4. As shown in Fig. 2(d) and Fig. S5(c) in the ESM, the bright white spots correspond to the pCDs, while the darker regions represent g-C_3N_4. The pCDs are clearly observed to be widely and uniformly distributed within the g-C_3N_4 framework. The HRTEM image was used to further confirm that the nanoparticles on 5pCDs-g-C_3N_4 are indeed pCDs, which exhibit well-defined lattice fringes with an interplanar spacing of 0.21 nm, embedded within the amorphous g-C_3N_4 (Fig. 2(e)). This lattice spacing is consistent with that of the pCDs prior to thermal polymerization, demonstrating the intimate integration of the pCDs into the g-C_3N_4 framework. The N_2 adsorption–desorption isotherms at 77 K were used to further analyze the microstructural features of 5pCDs-g-C_3N_4, including its specific surface area and pore structure. As shown in Fig. S7 in the ESM, the isotherms display a typical Type-IV curve with an H_3-Type hysteresis loop, indicating the presence of abundant mesopores. The calculated Brunauer–Emmett–Teller (BET) specific surface area of 5pCDs-g-C_3N_4 is 117.7 $m^2 \cdot g^{-1}$, showing a slight increase compared with pristine g-C_3N_4 (99.9 $m^2 \cdot g^{-1}$). In addition, relative to g-C_3N_4, 5pCDs-g-C_3N_4 exhibits a marked increase in pore density around 1.8 nm, along with the emergence of new mesopores centered at approximately 5.2 nm (Fig. S8 and Table S1 in the ESM). Zeta potential measurements indicate that the pCDs can modulate the surface charge environment. The 5pCDs-g-C_3N_4 still carries an overall negative surface charge, similar to g-C_3N_4; yet the absolute value is reduced due to the interaction with the positive surface charge of the incorporated pCDs (Fig. S9 in the ESM).

To analyze the surface chemical structures of 5pCDs-g-C_3N_4, the FT-IR spectroscopy was conducted, and g-C_3N_4 was used as a control. As shown in Fig. S10 in the ESM, the absorption peak at 800 cm^{-1} is attributed to the bending vibration of the triazine ring, while the bands in the range of 1200–1720 cm^{-1} correspond to the stretching vibrations of aromatic heterocycles (C–N and C=N). All samples exhibit these characteristic peaks, confirming that the g-C_3N_4 framework remains intact after the introduction of pCDs. Additionally, due to the low pCDs content and the overlap of their absorption features with those of g-C_3N_4, the characteristic peaks of the pCDs are not distinctly observed.

The metallized Co-5pCDs-g-C_3N_4 prepared from 5pCDs-g-C_3N_4 retains its original morphology (Fig. S11 in the ESM), and the elemental mapping results (Figs. 2(f)–2(i)) show that C, N, and Co are uniformly distributed across the nanosheets, confirming the homogeneous incorporation of cobalt ions into the composite. In addition, inductively coupled plasma-mass spectrometry (ICP-MS) analysis shows that the Co loading in Co-5pCDs-g-C_3N_4 is approximately 0.204 wt.% (Table S2 in the ESM). XRD analysis (Fig. 3(a)) reveals that g-C_3N_4, 5pCDs-g-C_3N_4, and Co-5pCDs-g-C_3N_4 display two characteristic diffraction peaks at about 27.9° and 13.0°, corresponding to the (002) and (100) planes of g-C_3N_4, respectively. These peaks arise from the interlayer stacking of aromatic planes and the in-plane periodicity of tri-s-triazine units. Notably, with the incorporation of pCDs, the (002) diffraction peak shifts from 27.9° to 27.8°, reflecting a slight expansion of the interlayer spacing in the modified materials (inset in Fig. 3(a)). This structural evolution is consistent with the observed increase in specific surface area and decrease in particle size of 5pCDs-g-C_3N_4, indicating that pCDs incorporation can effectively modulate the microstructure of g-C_3N_4. Importantly, no new diffraction peaks are observed after cobalt ions loading (Fig. 3(a)), suggesting that metal incorporation does not alter the crystalline structure of the 5pCDs-g-C_3N_4 framework.

To investigate the elemental composition and coordination environment of cobalt in Co-5pCDs-g-C_3N_4, X-ray photoelectron spectroscopy (XPS) was performed, with g-C_3N_4 and 5pCDs-g-C_3N_4 used as reference samples. Figure S12 in the ESM shows the survey XPS spectra of the three samples, in which only signals corresponding to C and N are observed, confirming that they share a similar elemental composition. The high-resolution C 1s spectrum of g-C_3N_4 (Fig. 3(b)) can be deconvoluted into three characteristic peaks located at 284.80, 286.03, and 288.08 eV, corresponding to C=C, C–O, and sp^2-hybridized carbon in the triazine ring (N=C–N), respectively [49]. The peak area at 284.80 eV increases from 4.69% for g-C_3N_4 to 6.00% for 5pCDs-g-C_3N_4 (Table S3 in the ESM), while the C/N atomic ratio slightly rises from 0.79 to 0.80 (Table S4 in the ESM). These results indicate the successful incorporation of pCDs into the g-C_3N_4 framework and preservation of the C=C structural integrity. The high-resolution N 1s spectrum of g-C_3N_4 (Fig. 3(c)) can be fitted into three main peaks centered at 398.60, 399.98, and 401.01 eV, assigned to sp^2-hybridized nitrogen in triazine rings (C–N=C), tertiary nitrogen (N–$(C)_3$), and terminal –NH_x groups, respectively. The relative intensity of the –NH_x peak increases from 12.10% for g-C_3N_4 to 14.75% for 5pCDs-g-C_3N_4 (Table S5 in the ESM), which may originate from surface –NH_x functionalities on pCDs. Moreover, the main C–N=C peak shifts slightly toward lower binding energy (from 398.60 to 398.53 eV), suggesting covalent coupling between pCDs and the g-C_3N_4 framework. For the Co 2p spectrum of the Co-5pCDs-g-C_3N_4 sample, two characteristic peaks appear at 781.80 and 797.00 eV (Fig. 3(d)), corresponding to Co(II) $2p_{3/2}$ and $2p_{1/2}$, respectively, confirming that the cobalt species predominantly exist in the +2 oxidation state. Moreover, the –NH_x peak shifts toward lower binding energy (Fig. 3(c)), implying the presence of interactions between –NH_x groups and Co ions, suggesting that the Co species are captured by the amino groups on the surface of the pCDs.

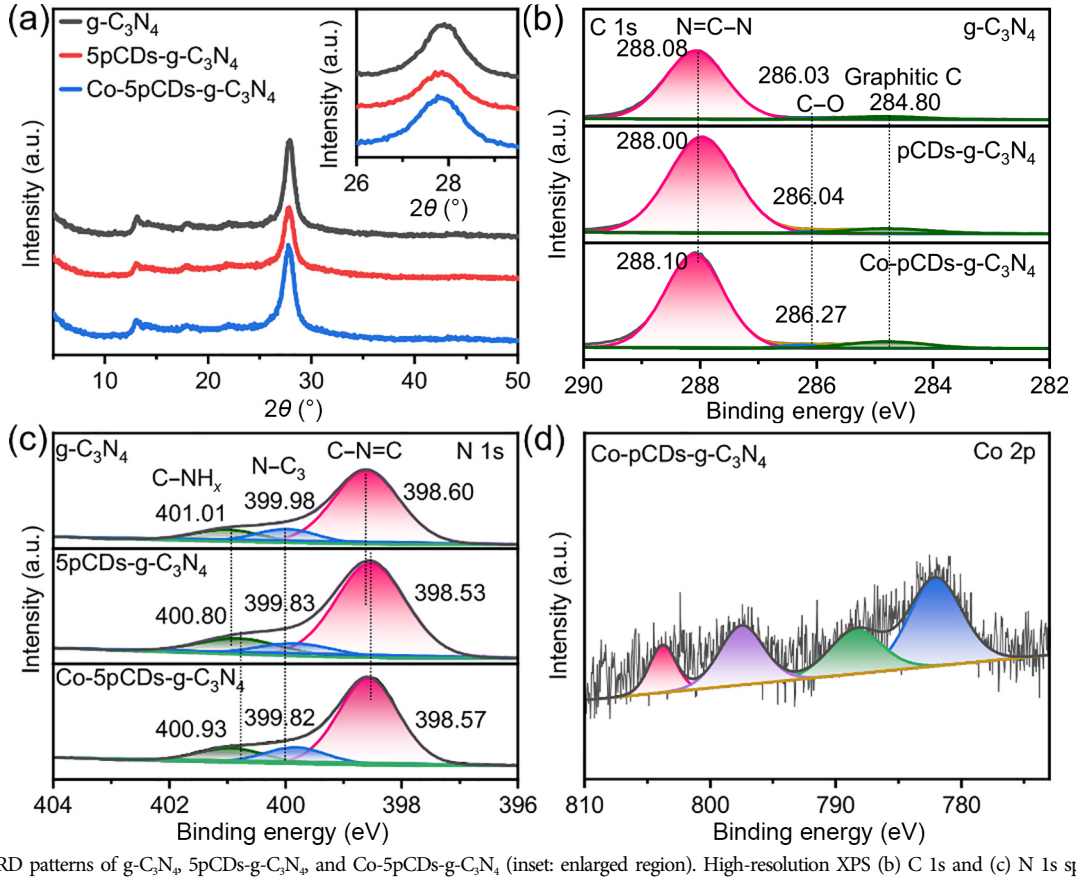

Figure 3 (a) XRD patterns of g-C_3N_4, 5pCDs-g-C_3N_4, and Co-5pCDs-g-C_3N_4 (inset: enlarged region). High-resolution XPS (b) C 1s and (c) N 1s spectra of g-C_3N_4, 5pCDs-g-C_3N_4, and Co-5pCDs-g-C_3N_4. (d) High-resolution XPS Co 2p spectrum of Co-5pCDs-g-C_3N_4.

3.2 Photocatalytic performance of Co-5pCDs-g-C_3N_4

The increased specific surface area and introduction of Co–N active sites are expected to enhance the photocatalytic CO_2 reduction activity. As a proof-of-concept, the photocatalytic performance of Co-5pCDs-g-C_3N_4 was evaluated in CH_3CN with TEOA as a sacrificial agent under irradiation from a 5 W light-emitting diode (LED) lamp. As shown in Fig. 4(a), the CO production rate reaches 616.1 μmol·g^{-1}·h^{-1}, with an H_2 production rate of 50.9 μmol·g^{-1}·h^{-1}, corresponding to a CO selectivity of 92%. Based on the measured Co loading, the time-dependent turnover number (TON) was calculated, as shown in Fig. S13 in the ESM. The TON for CO formation reaches 17 h^{-1}. To further elucidate the critical role of pCDs, a control sample (Co-g-C_3N_4) was prepared under identical conditions using pristine g-C_3N_4 as the support. The result indicates that pure g-C_3N_4 exhibits almost no photocatalytic activity (Fig. 4(b)), while Co-g-C_3N_4 shows only weak CO_2 reduction capability (6.8 μmol·g^{-1}·h^{-1}). ICP-MS analysis (Table S2 in the ESM) reveals that the Co loading in Co-5pCDs-g-C_3N_4 (0.204%) is 12 times higher than that in Co-g-C_3N_4 (0.016%), whereas the CO generation rate increases by approximately 91 times, confirming that cobalt ions coordinated via pCDs possess superior intrinsic catalytic activity. To investigate the effect of pCDs doping on catalytic performance, pCDs-CN samples with different pCDs contents are synthesized and used for photocatalytic CO_2 reduction. As shown in Fig. 4(c), the CO evolution rate increases gradually with the pCDs content, reaching a maximum at a pCDs loading of 5 mg. Beyond this threshold, the photocatalytic activity declines, likely due to the structural disruption of the g-C_3N_4 triazine framework, which hinders the charge separation and transfer. Furthermore, the cyclic stability test (Fig. 4(d)) shows a noticeable decrease in CO production after three consecutive cycles. Interestingly, re-metalization of the catalyst after five cycles almost fully restores its photocatalytic activity. ICP-MS measurements performed on the samples before and after re-metalization (Table S2 in the ESM) reveal that the cobalt content in the used catalyst decreases to 0.019%, significantly lower than that in the fresh Co-5pCDs-g-C_3N_4 (0.204%). After re-metalization, the Co content recovered to 0.179%, indicating that the loss of active Co species during the reaction was primarily responsible for the decreased activity. These results suggest that cobalt ions anchored by nitrogen-containing functional groups on the outer surface of pCDs are relatively unstable and may leach during the reaction, while the catalytic activity can be effectively restored through simple re-immobilization of metal ions. Moreover, the morphology of the sample after the reaction still exhibits visible CDs and nanosheet structures on the Co-5pCDs-g-C_3N_4 matrix, demonstrating the excellent photostability of the catalyst (Fig. S14 in the ESM).

To investigate the carbon source of CO produced in the photocatalytic experiments using Co-5pCDs-g-C_3N_4 as the catalyst, control experiments were conducted, including reactions in the dark, without TEOA, and an inert atmosphere such as N_2. As shown in Fig. 4(e), no CO was detected in the absence of light or TEOA. Similarly, when CO_2 was replaced with N_2, no CO signal was observed, indicating that CO formation depends on the synergistic effect of light, the catalyst, and the sacrificial agent. ^{13}C isotopic labeling combined with gas chromatography-mass spectrometry (GC-MS) provides a more direct and effective strategy

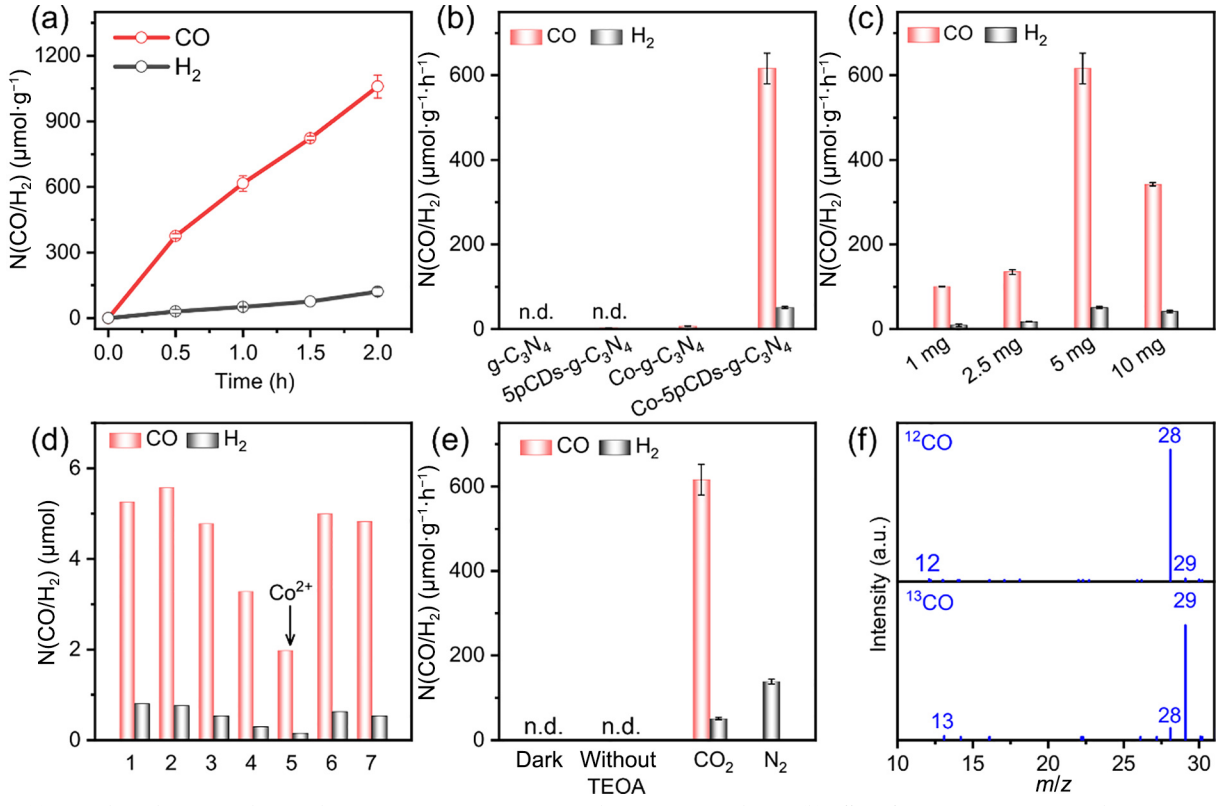

Figure 4 (a) Time-dependent CO and H_2 production over Co-5pCDs-g-C_3N_4 under 5 W LED irradiation. (b) Effect of Co incorporation on catalytic activity compared with pristine g-C_3N_4. (c) Performance comparison with different pCDs loadings. (d) Cycling stability of Co-5pCDs-g-C_3N_4 for CO_2 reduction, with metal reloading after the fifth cycle. (e) Control experiments under dark conditions, without sacrificial agent, or without CO_2. (f) GC-MS comparison of CO produced using CO_2 and $^{13}CO_2$ as feed gases.

for tracing the origin of CO_2 photoreduction products and ruling out interference from carbon contaminants in the photocatalyst or reaction system [50]. The retention time and component chromatograms (Fig. S15 in the ESM) show a peak at approximately 3 min corresponding to CO_2, while a small peak at around 15 min is assigned to CO. The GC-MS results show that the characteristic mass spectra of CO_2 and $^{13}CO_2$, corresponding to molecular ion peaks at m/z = 44 and 45, respectively, are presented in Fig. S16 in the ESM. Figure 4(f) presents the MS spectra of the main product, CO. Specifically, when $^{13}CO_2$ was used as the reactant gas, a signal at m/z = 29 corresponding to ^{13}CO was detected, whereas a signal at m/z = 28 corresponding to ^{12}CO was observed when $^{12}CO_2$ was used. The control experiments and isotopic tracing studies unambiguously demonstrate that the generated CO originates from the photocatalytic reduction of CO_2, rather than from the decomposition of the catalyst, sacrificial agent, or solvent.

3.3 Photophysical behaviors

To elucidate the intrinsic origin of the remarkably enhanced photocatalytic CO_2 reduction performance of the Co-5pCDs-g-C_3N_4 sample, the charge separation and transfer behaviors were systematically investigated to establish a rational structure–activity relationship. As shown in Fig. 5(a), the optical absorption properties of g-C_3N_4 and 5pCDs-g-C_3N_4 were analyzed by UV–vis diffuse reflectance spectroscopy (DRS). In the visible light range of 300–800 nm, the absorption edge of the pCDs-g-C_3N_4 sample exhibits a red shift with the incorporation of pCDs, indicating an effective modulation of the band structure and further confirming the successful incorporation of pCDs into the g-C_3N_4 framework. The corresponding Tauc-plots (Fig. S17 in the ESM) revealed that the bandgap decreased from 2.74 to 2.49 eV, consistent with the trend reported in previous literature. According to the Mott–Schottky plots (Fig. S18 in the ESM), the flat-band potentials (pH = 7, vs. NHE) of g-C_3N_4, 5pCDs-g-C_3N_4, and Co-5pCDs-g-C_3N_4 were determined to be −1.28, −1.25, and −1.15 V, respectively. The corresponding valence band positions were calculated to be 1.36, 1.14, and 1.02 V (Fig. 5(b)). Notably, the conduction band potentials of all three samples are more negative than the CO_2/CO reduction potential (−0.53 V), suggesting the thermodynamic feasibility of CO_2 reduction. PL spectra (Fig. 5(c)) further reveal the charge separation and recombination behaviors. Pristine g-C_3N_4 exhibits a strong emission peak at approximately 430 nm, indicating severe recombination. In contrast, the PL intensity of 5pCDs-g-C_3N_4 is markedly reduced, accompanied by the appearance of a new emission peak at 469 nm. This result suggests that the introduction of pCDs alters the carrier recombination pathways and constructs new electron transport channels between g-C_3N_4 and pCDs, thereby facilitating charge separation. Upon further coordination with cobalt ions, the PL intensity is further quenched, indicating an enhanced efficiency of charge separation and migration. Time-resolved photoluminescence (TRPL) decay curves (Fig. 5(d)) were fitted using a biexponential model (Table S6 in the ESM). The average lifetimes of g-C_3N_4, 5pCDs-g-C_3N_4, and Co-5pCDs-g-C_3N_4 were 5.32, 3.16, and 2.26 ns, respectively. The pronounced reduction in lifetime confirms that both pCDs incorporation and Co coordination accelerate the separation and transfer of photogenerated charge carriers. Photoelectrochemical (PEC) measurements (Fig. 5(e)) under intermittent light irradiation

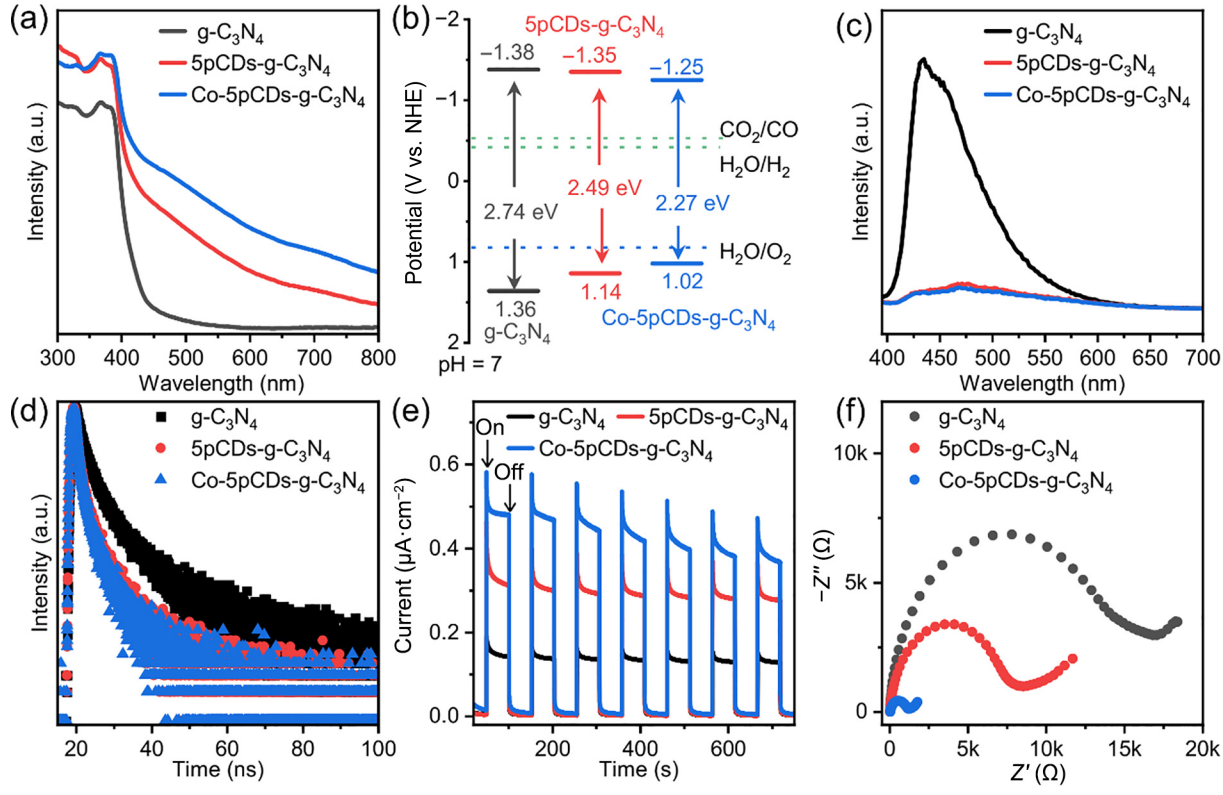

Figure 5 (a) UV–vis diffuse reflectance spectra of g-C_3N_4, 5pCDs-g-C_3N_4, and Co-5pCDs-g-C_3N_4. (b) Band structures of g-C_3N_4, 5pCDs-g-C_3N_4, and Co-5pCDs-g-C_3N_4. (c) Fluorescence emission spectra and (d) transient fluorescence lifetime spectra under 375 nm excitation of g-C_3N_4, 5pCDs-g-C_3N_4, and Co-5pCDs-g-C_3N_4. (e) Photocurrent density-time response curves and (f) electrochemical impedance spectra of g-C_3N_4, 5pCDs-g-C_3N_4, and Co-5pCDs-g-C_3N_4.

show that Co-5pCDs-g-C_3N_4 delivers the highest and most stable transient photocurrent density, significantly exceeding those of g-C_3N_4 and 5pCDs-g-C_3N_4. This finding demonstrates that the g-C_3N_4/pCDs interface forms an efficient charge transport channel, which promotes the directional transfer of electrons toward Co active centers. Electrochemical impedance spectroscopy (EIS, Fig. 5(f)) results further support this observation: Both 5pCDs-g-C_3N_4 and Co-5pCDs-g-C_3N_4 display a markedly smaller semicircle radius in the Nyquist plots, indicative of a reduced interfacial charge-transfer resistance. The lower resistance facilitates faster electron migration to the catalytic sites, favoring CO_2 activation and subsequent reduction reactions.

To further elucidate the ultrafast charge carrier dynamics, fs-TA spectroscopy was conducted to probe the carrier transfer behavior. As shown in Figs. 6(a), 6(d), and 6(g), the fs-TA contour plots display the time-resolved spectral evolution under 365 nm excitation. For pristine g-C_3N_4, an evident negative signal appears below 520 nm, which can be attributed to stimulated emission (SE) and ground-state bleaching (GSB) [51–53]. Meanwhile, a dominant positive signal emerges in the region of 550–750 nm, corresponding to excited-state absorption (ESA) of photogenerated electrons, holes, or electron–hole pairs. To gain further insight into the spectral evolution dynamics, the fs-TA spectra of g-C_3N_4, 5pCDs-g-C_3N_4, and Co-5pCDs-g-C_3N_4 at various delay time (0 ps–1 ns) are compared in Figs. 6(b), 6(e), and 6(h). Compared with pristine g-C_3N_4, the negative SE signals in 5pCDs-g-C_3N_4 and Co-5pCDs-g-C_3N_4 almost disappear, while the ESA region extends from 550–700 nm to a broader range of 470–750 nm. This spectral broadening highlights the markedly improved charge carrier separation and transfer dynamics induced by the co-anchoring of CDs on the g-C_3N_4 framework. To quantitatively analyze the decay kinetics of ESA, the transient absorption decay curves at representative wavelengths of 610 and 650 nm were fitted using a tri-exponential decay model (Figs. 6(c), 6(f), and 6(i)). The fitting parameters are summarized in Table S7 in the ESM. Compared with g-C_3N_4, the average lifetime of photoexcited carriers in 5pCDs-g-C_3N_4 is significantly prolonged from 53.75 to 74.14 ps at 610 nm, and 53.27 to 74.19 ps at 650 nm, indicating slower carrier recombination dynamics and a longer-lived shallow-trap carrier process. Upon Co incorporation, this effect is further enhanced, suggesting that the Co-N coordination promotes charge separation and prolongs carrier lifetimes (76.32 ps at 610 nm and 122.77 ps at 650 nm). These results collectively confirm that the formation of long-lived photoinduced electrons plays a dominant role in enhancing CO_2 photoreduction activity.

CO_2 temperature-programmed desorption (CO_2-TPD) was performed to probe the surface acid-base properties of g-C_3N_4 and Co-5pCDs-g-C_3N_4 and to elucidate the role of Co-5pCDs-g-C_3N_4 in CO_2 adsorption and activation. As shown in Fig. S19(a) in the ESM, the desorption feature at ~ 100 °C is assigned to physisorbed CO_2, whereas signals in the range of 200–300 °C correspond to chemisorbed species [54]. Compared with g-C_3N_4, Co-5pCDs-g-C_3N_4 exhibits a pronounced desorption peak shifted to higher temperatures (260–340 °C), indicating a stronger interaction with CO_2. Moreover, an additional high-temperature desorption peak appears for Co-5pCDs-g-C_3N_4 above 370 °C, which is absent for g-C_3N_4, suggesting the presence of newly introduced strong adsorption sites, plausibly associated with metal active centers. Density functional theory (DFT) calculations further support these observations. As shown in Fig. S20 in the ESM, the CO_2 adsorption

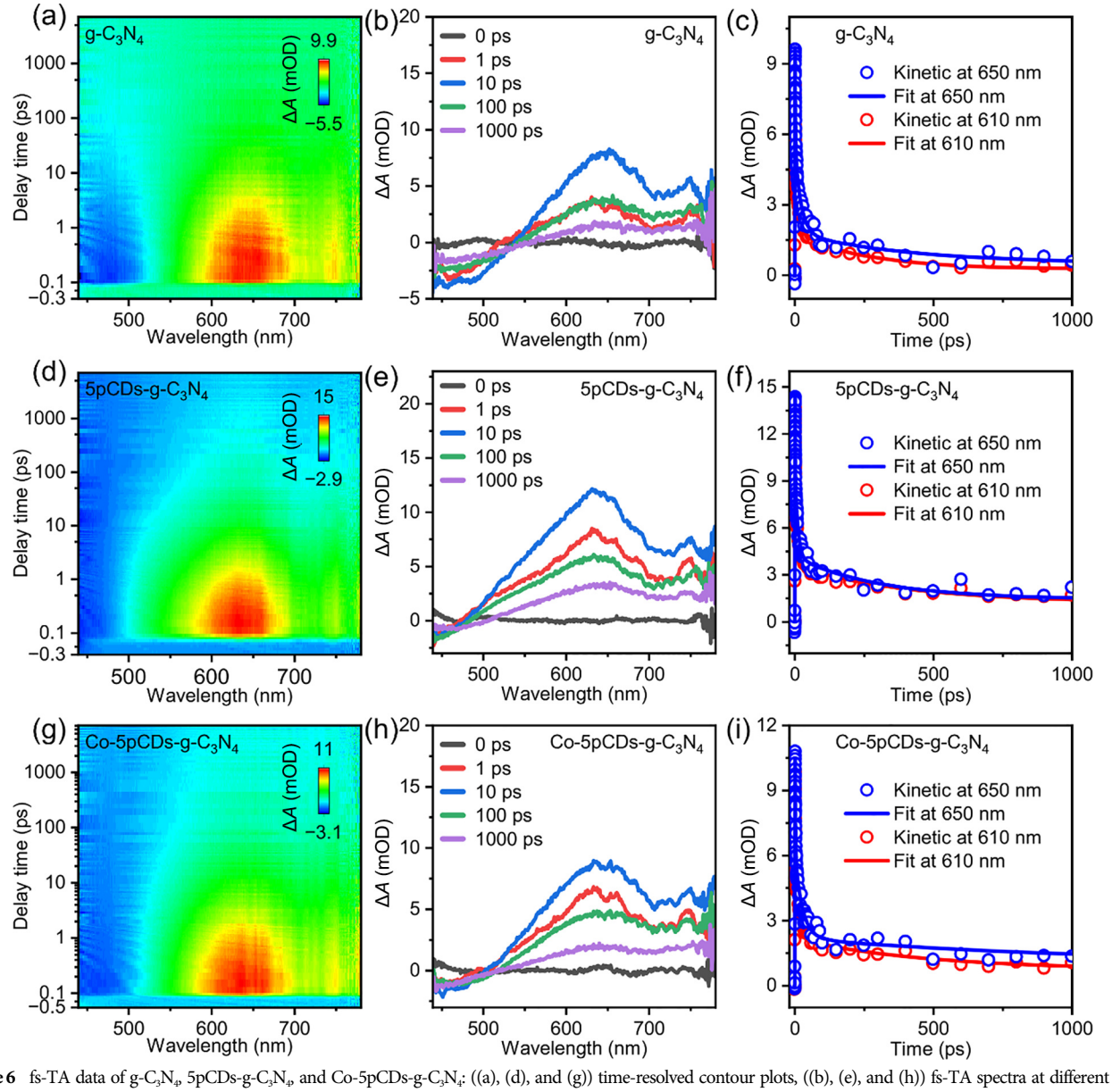

Figure 6 fs-TA data of g-C_3N_4, 5pCDs-g-C_3N_4, and Co-5pCDs-g-C_3N_4: ((a), (d), and (g)) time-resolved contour plots, ((b), (e), and (h)) fs-TA spectra at different delay times (0 ps–1 ns), and ((c), (f), and (i)) kinetic decay and fitting of excited-state absorption at 650 and 610 nm, respectively.

energy on Co-5pCDs-g-C_3N_4 (−1.29 eV) is higher than that on g-C_3N_4 (−0.32 eV), consistent with the CO_2-TPD results. CO-TPD was additionally conducted to gain mechanistic insight (Fig. S19(b) in the ESM). A distinct CO desorption feature appears below 100 °C, with Co-5pCDs-g-C_3N_4 exhibiting a lower desorption temperature than g-C_3N_4, indicating facilitated CO desorption. Taken together, these results suggest that Co-5pCDs-g-C_3N_4 enhances CO_2 adsorption and activation while promoting CO release, accounting for its superior catalytic performance.

In brief, the results from fs-TA, PL, TRPL, EIS, and photocurrent measurements collectively demonstrate that the synergistic integration of pCDs and Co active centers into the g-C_3N_4 framework remarkably enhances the separation and transfer efficiency of photogenerated charge carriers. This enhancement, coupled with the improved CO_2 adsorption/activation and facilitated product desorption evidenced by CO_2-TPD and CO-TPD analyses, ultimately accounts for the superior photocatalytic CO_2 reduction performance of the Co-5pCDs-g-C_3N_4 catalyst.

4 Conclusions

In summary, the photocatalyst Co-5pCDs-g-C_3N_4 was fabricated for the photocatalytic reduction of CO_2. Various characterizations were performed on g-C_3N_4, 5pCDs-g-C_3N_4, and Co-5pCDs-g-C_3N_4 to investigate their physicochemical properties and the transfer behavior and pathways of photogenerated charge carriers. The TEM and other characterization results confirm that the bottom-up copolymerization strategy enables the pCDs to be uniformly incorporated into the g-C_3N_4 framework, while the amino functional groups of the pCDs effectively anchor cobalt ions to form well-defined catalytic active centers. Meantime, the pCDs-induced modification of the g-C_3N_4 framework greatly promotes the charge separation, and the incorporation of cobalt ions further extends the charge-carrier lifetimes, collectively leading to a pronounced increase in the carrier lifetime of Co-5pCDs-g-C_3N_4. Therefore, the photocatalyst Co-5pCDs-g-C_3N_4 exhibited the highest photocatalytic performance, achieving a CO evolution rate

of 616.1 μmol·g^{-1}·h^{-1} with a selectivity of 92% over H_2, which represents an increase of 91 times compared with the Co-g-C_3N_4 catalyst, while maintaining excellent recyclability. Overall, this study not only provides new insights into the design of highly efficient photocatalysts for CO_2 reduction but also offers viable strategies for constructing and tuning the coordination environment of catalytic active centers.

Electronic Supplementary Material: Supplementary material (the details of all sample characterizations, electrochemical measurements, photoelectrochemical measurements, and photocatalytic CO_2 reduction, SEM/TEM images of 5pCDs-g-C_3N_4 and Co-5pCDs-g-C_3N_4, BET surface area and N_2 adsorption–desorption isotherms, pore-size distribution profiles of g-C_3N_4 and 5pCDs-g-C_3N_4, SEM/TEM images of Co-5pCDs-g-C_3N_4 after photocatalytic reaction, TON profiles of CO and H_2 over Co-5pCDs-g-C_3N_4, GC curves from ^{13}C isotopic tracing experiments, MS spectra of CO_2 and $^{13}CO_2$, Tauc-plots for bandgap determination, Mott–Schottky plots, surface elemental composition and relative proportions of surface C and N species from XPS, ICP analysis, PL decay, and fs-TA kinetic fitting results of g-C_3N_4, 5pCDs-g-C_3N_4, and Co-5pCDs-g-C_3N_4) is available in the online version of this article at https://doi.org/10.26599/NR.2026.94908500.

Data availability

All data needed to support the conclusions in the paper are presented in the manuscript and the Electronic Supplementary Material. Additional data related to this paper may be requested from the corresponding author upon request.

Acknowledgements

This work was financially supported by the National Natural Science Foundation of China (Nos. U25A20568 and U21A2085) and the Henan Province "Science and Technology Vice Governor" Three-Year Action Plan (2024–2026) of the Henan Provincial Department of Science and Technology.

Declaration of competing interest

All the contributing authors report no conflict of interests in this work.

Author contribution statement

S. D. C.: Data curation, project administration, validation, writing manuscript, experimental design. J. J. W.: Project administration, writing manuscript. T. W.: Writing – review & editing. S. H. L.: Auxiliary experimental operation. S. F. T.: Project administration, funding acquisition, writing manuscript. F. B.: Project administration, funding acquisition. All the authors have approved the final manuscript.

Use of AI statement

None.

References

[1] He, M. Z.; Cui, J. P.; Yi, Y. H.; Chen, H. W.; Zhang, Q.; Li, L. L.; Huang, L.; Hong, S. B. Vegetation increases global climate vulnerability risk by shifting climate zones in response to rising atmospheric CO_2. *Sci. Total Environ.* **2024**, *949*, 174810.

[2] Kan, F.; Xu, H.; Tang, S. C.; Peñuelas, J.; Lian, X.; Roebroek, C. T. J.; Anniwaer, N.; Wang, K.; Piao, S. L. Diminished biophysical cooling benefits of global forestation under rising atmospheric CO_2. *Nat. Commun.* **2025**, *16*, 4410.

[3] Wang, S. W.; Wang, L. G.; Wang, D. S.; Li, Y. D. Recent advances of single-atom catalysts in CO_2 conversion. *Energy Environ. Sci.* **2023**, *16*, 2759–2803.

[4] Lin, W.; Lin, F. W.; Lin, J.; Xiao, Z. W.; Yuan, D. Q.; Wang, Y. B. Efficient photocatalytic CO_2 reduction in ellagic acid-based covalent organic frameworks. *J. Am. Chem. Soc.* **2024**, *146*, 16229–16236.

[5] Guo, Z. G.; Yang, H. J.; Huang, X.; Ning, Y.; Luo, H.; Xie, J. H.; He, J. B.; Liu, Y. Y.; Lau, T. C. Highly efficient and selective photocatalytic CO_2 reduction to ethanol by Cu_4 clusters with adjacent Cu single atoms anchored on carbon nitride. *Angew. Chem., Int. Ed.* **2025**, *64*, e202423666.

[6] Fang, S. Y.; Rahaman, M.; Bharti, J.; Reisner, E.; Robert, M.; Ozin, G. A.; Hu, Y. H. Photocatalytic CO_2 reduction. *Nat. Rev. Methods Primers* **2023**, *3*, 61.

[7] Wang, X. C.; Maeda, K.; Chen, X. F.; Takanabe, K.; Domen, K.; Hou, Y. D.; Fu, X. Z.; Antonietti, M. Polymer semiconductors for artificial photosynthesis: Hydrogen evolution by mesoporous graphitic carbon nitride with visible light. *J. Am. Chem. Soc.* **2009**, *131*, 1680–1681.

[8] Wang, X. C.; Maeda, K.; Thomas, A.; Takanabe, K.; Xin, G.; Carlsson, J. M.; Domen, K.; Antonietti, M. A metal-free polymeric photocatalyst for hydrogen production from water under visible light. *Nat. Mater.* **2009**, *8*, 76–80.

[9] Yu, X. N.; Ng, S. F.; Putri, L. K.; Tan, L. L.; Mohamed, A. R.; Ong, W. J. Point-defect engineering: Leveraging imperfections in graphitic carbon nitride (g-C_3N_4) photocatalysts toward artificial photosynthesis. *Small* **2021**, *17*, 2006851.

[10] Rocha, G. F. S. R.; Da Silva, M. A. R.; Rogolino, A.; Diab, G. A. A.; Noleto, L. F. G.; Antonietti, M.; Teixeira, I. F. Carbon nitride based materials: More than just a support for single-atom catalysis. *Chem. Soc. Rev.* **2023**, *52*, 4878–4932.

[11] Che, W.; Zhao, S. L.; Byun, W. J.; Tao, T.; Jeon, J. P.; Zhao, Q. N.; Shao, Y. H.; Li, J.; Kim, J.; Lee, J. S. et al. From carbon nitrides to COFs: Opportunities and prospects in photocatalytic CO_2 reduction. *Adv. Mater.* **2025**, *37*, e06961.

[12] Tian, S. F.; Chen, S. D.; Ren, X. T.; Hu, Y. Q.; Hu, H. Y.; Sun, J. J.; Bai, F. An efficient visible-light photocatalyst for CO_2 reduction fabricated by cobalt porphyrin and graphitic carbon nitride via covalent bonding. *Nano Res.* **2020**, *13*, 2665–2672.

[13] Li, Y.; Li, X.; Zhang, H. W.; Xiang, Q. J. Porous graphitic carbon nitride for solar photocatalytic applications. *Nanoscale Horiz.* **2020**, *5*, 765–786.

[14] Chen, L.; Maigbay, M. A.; Li, M.; Qiu, X. Q. Synthesis and modification strategies of g-C_3N_4 nanosheets for photocatalytic applications. *Adv. Powder Mater.* **2024**, *3*, 100150.

[15] Hu, S.; Qiao, P. Z.; Yi, X. L.; Lei, Y. M.; Hu, H. L.; Ye, J. H.; Wang, D. F. Selective photocatalytic reduction of CO_2 to CO mediated by silver single atoms anchored on tubular carbon nitride. *Angew. Chem., Int. Ed.* **2023**, *62*, e202304585.

[16] Shang, Y. R.; Zheng, M.; Liu, H. J.; Jin, X. L.; Yan, C. S.; Song, L.; Qi, Z. M.; Jing, F. Y.; Song, P.; Zhou, X. et al. Mimicking frustrated lewis pairs on graphitic carbon nitride for CO_2 photoreduction. *ACS Catal.* **2023**, *13*, 14530–14539.

[17] Huang, Q. S.; Li, Q. J.; Chu, C. C.; Liu, Q.; Li, Z.; Mao, S. Synergetic regulation of electronic structure of graphitic carbon nitride through phosphorus and carbon co-doping for enhanced photocatalytic CO_2 reduction. *Chem. Eng. J.* **2024**, *482*, 149155.

[18] Zhao, J. H.; Wang, L.; Zhou, T. Y.; Yan, Y. H.; Sun, J. Q.; Hu, B.;

Liu, B.; Liu, C. B.; Che, G. B. Molecularly tunable donor-acceptor integrated carbon nitride for sunlight-driven H_2O_2 synthesis: Mechanism and performance insights. *Small* **2025**, *21*, 2500679.

[19] Li, Q. L.; Yang, D. Z.; Yin, Q. H.; Li, W. Y.; Yang, Y. L. Graphitic carbon nitride nanosheets decorated with Cu-doped carbon dots for the detection and degradation of phenolic pollutants. *ACS Appl. Nano Mater.* **2022**, *5*, 1925–1934.

[20] Zhu, D. D.; Zhou, Q. X. Nitrogen doped g-C_3N_4 with the extremely narrow band gap for excellent photocatalytic activities under visible light. *App. Catal. B: Environ.* **2021**, *281*, 119474.

[21] Sun, X. H.; Shi, Y. X.; Lu, J. L.; Shi, W. L.; Guo, F. Template-free self-assembly of three-dimensional porous graphitic carbon nitride nanovesicles with size-dependent photocatalytic activity for hydrogen evolution. *Appl. Surf. Sci.* **2022**, *606*, 154841.

[22] Li, Q.; Jiao, Y. Q.; Tang, Y. Q.; Zhou, J.; Wu, B. G.; Jiang, B. J.; Fu, H. G. Shear stress triggers ultrathin-nanosheet carbon nitride assembly for photocatalytic H_2O_2 production coupled with selective alcohol oxidation. *J. Am. Chem. Soc.* **2023**, *145*, 20837–20848.

[23] Dos Santos, G.; Tian, L.; Gonçalves, R.; García, H.; Rossi, L. Boosting CO_2 photoreduction efficiency of carbon nitride via S-scheme g-C_3N_4/Fe_2TiO_5 heterojunction. *Adv. Funct. Mater.* **2025**, *35*, 2422055.

[24] Su, L. N.; Wang, P. F.; Li, M. M.; Zhao, Z. Y.; Li, Y.; Zhan, S. H. Synergistic enhancement of photocatalytic molecular oxygen activation by nitrogen defect and interfacial photoelectron transfer over Z-scheme α-Fe_2O_3/g-C_3N_4 heterojunction. *App. Catal. B: Environ.* **2023**, *335*, 122890.

[25] Fu, J. W.; Yu, J. G.; Jiang, C. J.; Cheng, B. g-C_3N_4-based heterostructured photocatalysts. *Adv. Energy Mater* **2018**, *8*, 1701503.

[26] Seng, R. X.; Tan, L. L.; Lee, W. P. C.; Ong, W. J.; Chai, S. P. Nitrogen-doped carbon quantum dots-decorated 2D graphitic carbon nitride as a promising photocatalyst for environmental remediation: A study on the importance of hybridization approach. *J. Environ. Manage.* **2020**, *255*, 109936.

[27] Abdellatif, H. R. S.; Zhang, G.; Wang, X. T.; Xie, D. T.; Irvine, J. T. S.; Ni, J. P.; Ni, C. S. Boosting photocatalytic oxidation on graphitic carbon nitride for efficient photocatalysis by heterojunction with graphitic carbon units. *Chem. Eng. J.* **2019**, *370*, 875–884.

[28] Morbiato, L.; Cardo, L.; Sturabotti, E.; Gobbo, P.; Filippini, G.; Prato, M. Structure matters: Tailored graphitization of carbon dots enhances photocatalytic performance. *ACS Nano* **2025**, *19*, 4887–4900.

[29] Liu, Y. Q.; Zhu, C. J.; Sun, J. W.; Ge, Y.; Song, F. J.; Wang, G. Z.; Xu, Q. Efficient photocatalytic degradation of volatile organic compounds over carbon quantum dots decorated Bi_2WO_6 under visible light. *Environ. Sci. Pollut. Res.* **2021**, *28*, 25949–25958.

[30] Xu, W. G.; Xu, Q. H.; Liu, M. R.; Shan, H. B.; Bi, X. Z.; Zhang, Q.; Ai, J. S.; Liu, Q.; Wu, M. B. Molecularly tuned carbon dots for visible-light-driven boryl radical generation via enhanced hole transfer. *J. Am. Chem. Soc.* **2025**, *147*, 35019–35030.

[31] Ouyang, L. F.; Ng, M.; Zhou, Z. H.; Wu, H.; Tang, M. C.; Chen, S. S. Manipulating charge dynamics in carbon nitride by carbon dot doping for efficient photocatalysis. *Adv. Sci.* **2025**, *12*, 2417390.

[32] Guo, H. Z.; Zhou, L.; Huang, K.; Li, Y. Q.; Hou, W. D.; Liao, H. G.; Lian, C.; Yang, S. W.; Wu, D. L.; Lei, Z. D. et al. Nitrogen-rich carbon dot-mediated n→π* electronic transition in carbon nitride for superior photocatalytic hydrogen peroxide production. *Adv. Funct. Mater.* **2024**, *34*, 2402650.

[33] Dong, J. X.; Liu, G. X.; Petrov, Y. V.; Feng, Y. J.; Jia, D. C.; Baulin, V. E.; Tsivadze, A. Y.; Zhou, Y.; Li, B. Q. EDTA-functionalized carbon dots-metal nanozymes based on coordination chemistry: Species of metal ions determines enzyme-mimicking catalyzed activities. *ACS Mater. Lett.* **2024**, *6*, 1112–1119.

[34] Dong, J. X.; Li, B. Q.; Xiao, J.; Liu, G. X.; Baulin, V.; Feng, Y. J.; Jia, D. C.; Tsivadze, A. Y.; Zhou, Y. Carbon dots with tailor-made chelating ligands for specific metal ions recognition: Target synthesis and prediction of metal ions selectivity. *Carbon* **2022**, *199*, 151–160.

[35] Ouyang, Y.; Biniuri, Y.; Fadeev, M.; Zhang, P.; Carmieli, R.; Vázquez-González, M.; Willner, I. Aptamer-modified Cu^{2+}-functionalized C-dots: Versatile means to improve nanozyme activities—"Aptananozymes". *J. Am. Chem. Soc.* **2021**, *143*, 11510–11519.

[36] Ren, Z. X.; Zhao, B.; Xie, J. Designing N-confused metalloporphyrin-based covalent organic frameworks for enhanced electrocatalytic carbon dioxide reduction. *Small* **2023**, *19*, e2301818.

[37] Zhang, Q.; Gao, S. Q.; Guo, Y. Y.; Wang, H. Y.; Wei, J. S.; Su, X. F.; Zhang, H. C.; Liu, Z. M.; Wang, J. J. Designing covalent organic frameworks with Co-O_4 atomic sites for efficient CO_2 photoreduction. *Nat. Commun.* **2023**, *14*, 1147.

[38] Yuan, H. Q.; Du, J. H.; Ming, M.; Chen, Y.; Jiang, L.; Han, Z. J. Combination of organic dye and iron for CO_2 reduction with pentanuclear Fe_2Na_3 purpurin photocatalysts. *J. Am. Chem. Soc.* **2022**, *144*, 4305–4309.

[39] Zhu, Y. R.; Xue, Y. L.; Wang, Z.; Chao, D. B. Robust noble metal-free photoconversion of CO_2 to CO with a molecule/MOF hybrid catalyst for straightforward two-chamber organic carbonylation. *ACS Catal.* **2025**, *15*, 3546–3557.

[40] Zhang, H. G.; Liu, S. Z.; Zhou, X. L.; Zheng, Z. K.; Wang, P.; Cheng, H. F.; Wang, Z. Y.; Dai, Y.; Liu, Y. Y.; Huang, B. B. Enhanced selectivity of photocatalytic CO_2 reduction to formate via tailoring the metal site. *ACS Catal.* **2025**, *15*, 3000–3007.

[41] Ding, C.; Lu, X. X.; Tao, B.; Yang, L. Q.; Xu, X. Y.; Tang, L. Q.; Chi, H. Q.; Yang, Y.; Meira, D. M.; Wang, L. et al. Interlayer spacing regulation by single-atom $indium^{\delta+}$-N_4 on carbon nitride for boosting CO_2/CO photo-conversion. *Adv. Funct. Mater.* **2023**, *33*, 2302824.

[42] Ou, H. H.; Ning, S. B.; Zhu, P.; Chen, S. H.; Han, A. L.; Kang, Q.; Hu, Z. F.; Ye, J. H.; Wang, D. S.; Li, Y. D. Carbon nitride photocatalysts with integrated oxidation and reduction atomic active centers for improved CO_2 conversion. *Angew. Chem., Int. Ed.* **2022**, *61*, e202206579.

[43] P, S.; John, J.; Rajan, T. P. D.; Anilkumar, G. M.; Yamaguchi, T.; Pillai, S. C.; Hareesh, U. S. Graphitic carbon nitride (g-C_3N_4) based heterogeneous single atom catalysts: Synthesis, characterisation and catalytic applications. *J. Mater. Chem. A* **2023**, *11*, 8599–8646.

[44] Zhao, S. Q.; Tang, Z. Y.; Guo, S. J.; Han, M. M.; Zhu, C.; Zhou, Y. J.; Bai, L.; Gao, J.; Huang, H.; Li, Y. Y. et al. Enhanced activity for CO_2 electroreduction on a highly active and stable ternary Au-CDots-C_3N_4 electrocatalyst. *ACS Catal.* **2018**, *8*, 188–197.

[45] Ji, C. Y.; Han, Q. R.; Zhou, Y. Q.; Wu, J. J.; Shi, W. Q.; Gao, L. P.; Leblanc, R. M.; Peng, Z. L. Phenylenediamine-derived near infrared carbon dots: The kilogram-scale preparation, formation process, photoluminescence tuning mechanism and application as red phosphors. *Carbon* **2022**, *192*, 198–208.

[46] Wang, Q.; Pu, Z. X.; Wang, Y.; Li, M. T. Surface passivated *p*-phenylenediamine carbon quantum dots (p-CQDs) as fluorescent turn-on probes for the detection of Li^+ and L-arginine by two different mechanisms. *Opt. Mater.* **2023**, *136*, 113415.

[47] Zheng, X. C.; Ren, S. T.; Gai, Q. X.; Liu, W. J. Carbon dot/carbon nitride composites fluorescent probe for the highly selective detection of Cr(VI) ions. *J. Photochem. Photobiol. A: Chem.* **2020**, *400*, 112711.

[48] Hasan, M.; Baheerathan, B.; Sutradhar, S.; Shahbandinejad, R.; Rakshit, S.; Kozinski, J.; Li, D. B.; Hu, Y. L.; Kang, K. Microwave-assisted synthesis of biomass-derived N-doped carbon dots for metal ion sensing. *Carbon Res.* **2025**, *4*, 49.

[49] Ma, B.; Chen, G.; Fave, C.; Chen, L. J.; Kuriki, R.; Maeda, K.; Ishitani, O.; Lau, T. C.; Bonin, J.; Robert, M. Efficient visible-light-

driven CO_2 reduction by a cobalt molecular catalyst covalently linked to mesoporous carbon nitride. *J. Am. Chem. Soc.* **2020**, *142*, 6188–6195.

[50] Wang, S. Y.; Jiang, B.; Henzie, J.; Xu, F. Y.; Liu, C. Y.; Meng, X. G.; Zou, S. R.; Song, H.; Pan, Y.; Li, H. X. et al. Designing reliable and accurate isotope-tracer experiments for CO_2 photoreduction. *Nat. Commun.* **2023**, *14*, 2534.

[51] Khan, M. A.; Maity, P.; Al-Oufi, M.; Al-Howaish, I. K.; Idriss, H. Electron transfer of the metal/semiconductor system in photocatalysis. *J. Phys. Chem. C* **2018**, *122*, 16779–16787.

[52] Yang, W. X.; Godin, R.; Kasap, H.; Moss, B.; Dong, Y. F.; Hillman, S. A. J.; Steier, L.; Reisner, E.; Durrant, J. R. Electron accumulation induces efficiency bottleneck for hydrogen production in carbon nitride photocatalysts. *J. Am. Chem. Soc.* **2019**, *141*, 11219–11229.

[53] Xiao, X. D.; Ruan, Z. S. L.; Li, Q.; Zhang, L. P.; Meng, H. Y.; Zhang, Q.; Bao, H. L.; Jiang, B. J.; Zhou, J.; Guo, C. Y. et al. A unique Fe-N_4 coordination system enabling transformation of oxygen into superoxide for photocatalytic C–H activation with high efficiency and selectivity. *Adv. Mater.* **2022**, *34*, 2200612.

[54] Wang, H. N.; Song, L.; Lv, X. M.; Wang, H. Z.; Zhang, F.; Hao, S. Y.; Wei, R. L.; Zhang, L. J.; Han, Q.; Zheng, G. F. Low-coordination triangular Cu_3 motif steers CO_2 photoreduction to ethanol. *Angew. Chem., Int. Ed.* **2025**, *64*, e202500928.